Supplementary information

Coherent spin-wave transport in an antiferromagnet

In the format provided by the
authors and unedited

Supplementary Information

Coherent spin-wave transport in an antiferromagnet

J.R. Hortensius[1‡*], D. Afanasiev[1‡], M. Matthiesen[1], R. Leenders[2], R. Citro[3], A.V. Kimel[4], R.V. Mikhaylovskiy[2], B.A. Ivanov[5], and A.D. Caviglia[1§]

[1]*Kavli Institute of Nanoscience, Delft University of Technology, P.O. Box 5046, 2600 GA Delft, The Netherlands.*
[2]*Department of Physics, Lancaster University, Bailrigg, Lancaster LA1 4YW, United Kingdom*
[3]*Dipartimento di Fisica "E.R. Caianiello", Università di Salerno and Spin-CNR, I-84084 Fisciano (Sa), Italy*
[4]*Radboud University Nijmegen, Institute for Molecules and Materials, 6525 AJ Nijmegen, The Netherlands.*
[5]*Institute of Magnetism, National Academy of Sciences and Ministry of Education and Science, 03142 Kyiv, Ukraine.*

*Correspondence to: j.r.hortensius@tudelft.nl, dmytro.afanasiev@physik.uni-regensburg.de or a.caviglia@tudelft.nl

‡These authors contributed equally to this work

S1. Theory for magneto-optical detection of propagating spin waves in antiferromagnets

S1.1 Magnetic potential

The antiferromagnetic order can be best described by introducing the antiferromagnetic Néel vector $\mathbf{L} = \mathbf{M}_1 - \mathbf{M}_2$ and net magnetization $\mathbf{M} = \mathbf{M}_1 + \mathbf{M}_2$, where $\mathbf{M}_{1,2}$ are the magnetizations of the antiferromagnetically coupled magnetic sublattices, such that $|\mathbf{M}_1| = |\mathbf{M}_2| = M_0$ and $|\mathbf{L}| \approx 2M_0 = L_0$.

The density of magnetic energy in $DyFeO_3$ written in terms of $\mathbf{M}$ and $\mathbf{L}$ reads[1,2]:

$$w(\mathbf{M}, \mathbf{L}) = \frac{H_{ex}}{2M_0}\mathbf{M}^2 - (\mathbf{H}_0 \cdot \mathbf{M}) - \frac{H_D}{2M_0}\left(e_y \cdot [\mathbf{L} \times \mathbf{M}]\right) + w_a(\mathbf{L}). \tag{S1.1}$$

In this expression, H_{ex} is the effective exchange field ($\omega_{ex} = 2\gamma H_{ex}$), with $\gamma = 1.76 \ 10^7 \ \text{s}^{-1}\text{Oe}^{-1}$ the gyromagnetic ratio, $\mathbf{H}_0$ is the external magnetic field, H_D is the magnitude of the effective Dzyaloshinskii-Moriya field ($\mathbf{H}_D = \frac{H_D}{2M_0}[e_y \times \mathbf{L}]$, e_y is the unit vector along the y-axis, which corresponds to the even C_2 crystal axis in $DyFeO_3$). The spontaneous spin-reorientation between the two competing magnetic states is governed by the temperature-dependence of the energy of the magneto-crystalline anisotropy $w_a(\mathbf{L})$ [3,4]:

$$w_a(\mathbf{L}) = \frac{1}{2}K_2(T)L_y^2 - \frac{1}{2}K_4 L_y^4, \tag{S(1.2)}$$

with $K_{2,4}$ phenomenological parameters that describe the strength of the magnetic anisotropy.

Within the sigma-model approach, the dynamics of the Néel vector is described by a closed equation (sigma-model equation, see, e.g., review article [2] and Supplementary Section S2 for details), whereas the net magnetization $\mathbf{M}$ is determined by this vector and its time derivative via the relation:

$$\mathbf{M} = \frac{M_0}{H_{ex}}\mathbf{H}_D + \frac{1}{2M_0\omega_{ex}}\left[\frac{\partial \mathbf{L}}{\partial t} \times \mathbf{L}\right]. \tag{S1.3}$$

In $DyFeO_3$ the ground state of the Néel vector as well as its dynamics corresponding to the quasi-antiferromagnetic mode (q-AFM) is restricted to the *(xy)* plane. For such dynamics, the Néel vector

can be parametrized by introducing the angle φ_L that the vector forms with the y-axis, $\mathbf{L}=L_0(\sin\varphi_L, \cos\varphi_L, 0)$. In the ground state of DyFeO$_3$:

$$\varphi_L = \begin{cases} 0, & T < T_M \\ \dfrac{\pi}{2}, & T > T_M \end{cases} \tag{S1.4}$$

For such planar dynamics, the net magnetization M_z emerges along the z-axis, such that:

$$M_z = \frac{M_0}{H_{ex}}\left(-H_D \sin\varphi_L + \frac{1}{\gamma}\frac{\partial\varphi_L}{\partial t}\right), \tag{S1.5}$$

At this point we introduce a variable φ to designate deviations of the vector $\mathbf{L}$ from the equilibrium orientation, such that $\varphi = \varphi_L$ for the collinear AFM state and $\varphi = \pi/2 - \varphi_L$ for the canted AFM state. For the case of small deviations of the Néel vector from equilibrium, we assume $\varphi \ll 1$ and obtain:

$$M_z = \begin{cases} \dfrac{M_0}{H_{ex}}\left(-H_D\varphi + \dfrac{1}{\gamma}\dfrac{\partial\varphi}{\partial t}\right), & T < T_M \\ \dfrac{M_0}{H_{ex}}\left(-H_D - \dfrac{1}{\gamma}\dfrac{\partial\varphi}{\partial t}\right), & T > T_M \end{cases} \tag{S1.6}$$

S1.2 Magneto-optical detection mechanism for the finite-k magnon modes

Optical detection of magnetization dynamics in a reflection geometry is performed using the magneto-optical Kerr effect (MOKE). The phenomenon originates from a helicity-dependent refractive index in the material with broken time reversal symmetry. The refractive index differs for left-handed and right-handed polarized light, resulting in different reflection coefficients. To calculate the rotation of the plane of polarization after reflection, linearly polarized light is first decomposed into circularly polarized components. For simplicity, it is assumed that the incident light is polarized along the x-axis, and the normalized electric field vector $\boldsymbol{e}_i$ in the (xy) plane is:

$$\boldsymbol{e}_i = \frac{1}{2}\begin{pmatrix} 1 \\ -i \end{pmatrix} + \frac{1}{2}\begin{pmatrix} 1 \\ +i \end{pmatrix} = \frac{1}{2}\boldsymbol{e}^+ + \frac{1}{2}\boldsymbol{e}^-, \tag{S1.7}$$

where $\boldsymbol{e}^{\pm} = \begin{pmatrix} 1 \\ \mp i \end{pmatrix}$. Then the reflected field is

$$\boldsymbol{e}_r = \frac{1}{2}r^+\boldsymbol{e}^+ + \frac{1}{2}r^-\boldsymbol{e}^- = \frac{1}{2}\begin{pmatrix} r^+ + r^- \\ i(r^- - r^+) \end{pmatrix}, \tag{S1.8}$$

3

Now the reflectivity is written as the sum of the static reflectivity r_0 and the dynamic part of the reflectivity Δr, which is induced by the spin wave:

$$r^+ = r_0^+ + \Delta r^+ \qquad \text{(S1.9)}$$
$$r^- = r_0^- + \Delta r^-$$

We consider the experimental geometry schematically shown in Suppl. Fig. 1a, in which a probe pulse enters the material at $z = 0$. To find the change in reflectivity, depending on the light helicity, we take an approach similar to the ultrafast detection of acoustic phonons, where phonon-induced strain affects reflectivity [see Ref. [5], Eq. (32)]. In Ref. [5] the change in reflectivity is derived as function of the time and space dependent change in permittivity $\Delta\varepsilon(z,t)$ due to the strain modulation. Here, the same equation is employed to calculate the change of reflectivity induced by magnetization. The equation taken from Ref. [5] reads:

$$r = r_0 + \frac{ik_0^2}{2k} t_0 \tilde{t}_0 \int_0^\infty \mathrm{d}z' \, e^{2ikz'} \Delta\varepsilon(z',t), \qquad \text{(S1.10)}$$

where r_0 is the reflection coefficient in absence of perturbations in the permittivity, t_0 is the transmission coefficient of the light into the medium, and $\tilde{t}_0$ is the transmission coefficient from the medium into free space, k_0 is the wave-vector of the light in free space and k is the wave-vector of light in the medium.
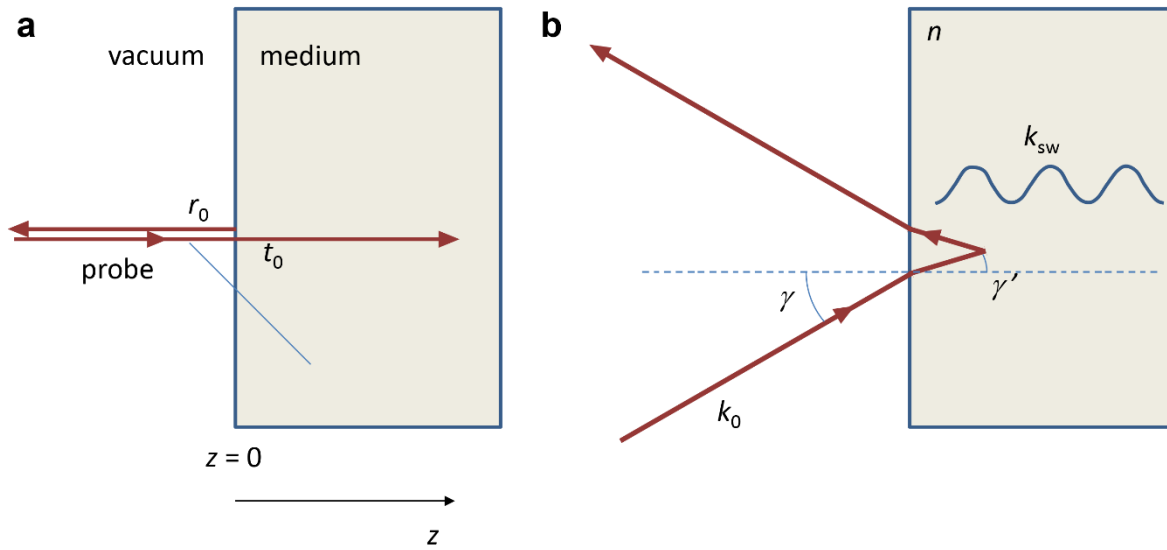
Supplementary Figure 1: **Experimental geometry to probe spin-wave excitations**. (**a**) Schematic diagram of the experiment considered. (**b**) Schematic illustration of the detection condition from Eq. (2) in the main text.

Two electromagnetic eigenmodes exist in a magnetic material with (dynamical) magnetization along the z-axis, which have left-handed and right-handed circular polarization ($\pm$) and experience different refractive indices $n_\pm$[6]. From these effective refractive indices, the effective permittivity modulation $\Delta\varepsilon$ can be obtained:

$$n_\pm^2 = \varepsilon \pm g = \varepsilon + \Delta\varepsilon_\pm, \tag{S1.11}$$

where g is the gyration term. Generally, this gyration term is proportional to the net magnetization: $g(M) = aM_z$, where a is a proportionality coefficient. From this it is found that:

$$\Delta\varepsilon_\pm(z, t) = \pm aM_z(z, t) \tag{S1.12}$$

Inserting the expression for $\Delta\varepsilon(z, t)$ in Eq. (S1.9) for right- and left-handed circular polarization we obtain:

$$
\begin{aligned}
r^+ &= r_0^+ - it_0^+ \tilde{t}_0^+ \frac{ak_0^2}{2k^+} \int_0^\infty dz' e^{2ik^+ z'} M_z(z', t) \equiv r_0^+ + \Delta r^+ \\
r^- &= r_0^- + it_0^- \tilde{t}_0^- \frac{ak_0^2}{2k^-} \int_0^\infty dz' e^{2ik^- z'} M_z(z', t) \equiv r_0^- + \Delta r^-
\end{aligned}
\tag{S1.13}
$$

For the sake of simplicity, we use the approximation of a pure antiferromagnet, such that the difference in reflection coefficients, transmission coefficients and wave vectors of light with opposite helicity in statics is negligible (we also neglect higher-order effects such as magnetic birefringence), simplifying the expression to:

$$r^+ = r_0 - \Delta r$$
$$r^- = r_0 + \Delta r \quad , \tag{S1.14}$$

where

$$\Delta r = i\frac{ak_0^2}{2k}t_0\tilde{t}_0\int_0^\infty \mathrm{d}z' e^{2ikz'}M_z(z',t). \tag{S1.15}$$

Now the rotation angle θ_K is calculated from equation (S1.8), by taking the ratio of the y- and x-components. Generally, the rotation angles are small such that $\tan(\theta_K) \approx \theta_K$ so that:

$$\theta_K \approx \frac{i(r^- - r^+)}{r^- + r^+} = \frac{i\Delta r}{r_0} \tag{S1.16}$$

As discussed in the manuscript and Supplementary Section S2, the optical pumping results in the excitation of a broadband spin-wave wave packet. We consider an arbitrary plane spin wave component of the packet with the frequency ω_s and the wavevector $k_m(\omega_s)$. We show below that the experimentally detected spin wave component is fully defined by the wavevector k of the probe pulse.

Following Eqs. S1.5, S1.6, spin dynamics in DyFeO$_3$ results in an oscillatory out-of-plane magnetization. The magnetization M_z associated with the propagating spin wave can thus be written as follows:

$$M_z(z,t) = M_k e^{i\omega_s t} e^{-ik_m(\omega_s)z} \tag{S1.17}$$

Here, M_k is the amplitude of the chosen spin wave component, determined by the amplitude of the spin deflection φ, (see Eqs. (S1.5, S1.6)) and $k_m(\omega_s)$ is the wave-vector of the spin wave, related to ω_s through the dispersion relation ω_k.

Substituting Eq. (S1.17) in Eq. (S1.15) and in Eq. (S1.16) afterwards, results in the following expression for the rotation angle:

$$\theta_K = \frac{t_0 \tilde{t}_0}{r_0} \frac{a k_0^2}{2k} M_k \int_0^\infty dz e^{i\omega_s t} e^{i(2k - k_m(\omega_s))z}. \tag{S1.18}$$

Note that in a general case $k_m = \kappa_m - i\eta_m$, i.e. spin waves decay upon propagation from the sample boundary with a decrement η_m. For the case $\eta_m \neq 0$ the integral S1.18 converges and the result is:

$$\theta_K = i \frac{t_0 \tilde{t}_0}{r_0} \frac{a k_0^2}{2k} M_k e^{i\omega_s t} \left(\frac{1}{2k - k_m(\omega_s)} \right) \tag{S1.19}$$

The fraction $\left(\frac{1}{2k - k_m(\omega_s)} \right)$ can be expressed as:

$$\left(\frac{1}{2k - k_m(\omega_s)} \right) = \frac{2k - \kappa_m(\omega_s)}{\left(2k - \kappa_m(\omega_s) \right)^2 + \eta_m^2} - \frac{i\eta_m}{\left(2k - \kappa_m(\omega_s) \right)^2 + \eta_m^2} \tag{S1.20}$$

Now we can assume $\eta_m \ll \kappa_m$ and take the limit $\eta_m \to 0$. Taking into account one of the definitions of the Dirac function $\pi\delta(x) = \lim_{a\to 0} \frac{a}{x^2 + a^2}$ we obtain:

$$\lim_{\eta_m \to 0} \left(\frac{1}{2k - k_m(\omega_s)} \right) = \frac{1}{\left(2k - \kappa_m(\omega_s) \right)} - i\pi\delta\left(2k - \kappa_m(\omega_s) \right) \tag{S1.21}$$

Equations (S1.19) and (S1.21) select the spin waves with wave vectors satisfying the expression $2k - k_m(\omega_s) = 0$ to be detected as $\theta_K \sim \delta\left(2k - k_m(\omega_s) \right)$, assuming $\kappa_m = k_m$ in the limit of no spin wave damping and taking the real part of θ_K, which corresponds to the polarization rotation. If one rewrites this expression in terms of the wavelengths $2\lambda_m = \lambda_{probe}$, with λ_m the wavelength of the spin wave and λ_{probe} the wavelength of the probe pulse in the medium, the well-known Bragg condition is obtained. In the specific case of our experiment, the gradient of the excitation is directed in the z-direction which, as discussed in Supplementary Section S2, results in spin waves with a wavevector in this particular direction. In the experiment, however, the incoming probe pulse can be directed under a certain angle γ. Taking refraction into account (see Suppl. Fig. 1b), which leads to a refracted angle γ' for the incoming probe pulse, the detection expression becomes:

$$k_m = 2k_0 n \cos\gamma', \tag{S1.22}$$

which is Eq. (2) in the main text.

The result is the following. Assuming a spin wave packet distribution as discussed in Supplementary Section S2 (see Suppl. Fig. 2a), the reflection geometry provides a sharp sensitivity

to a single component, depending on the probe photon wavenumber. As a result, the oscillation emerging in the time-resolved probe polarization (Suppl. Fig. 2b) has the frequency of the spin wave at that particular wavenumber.
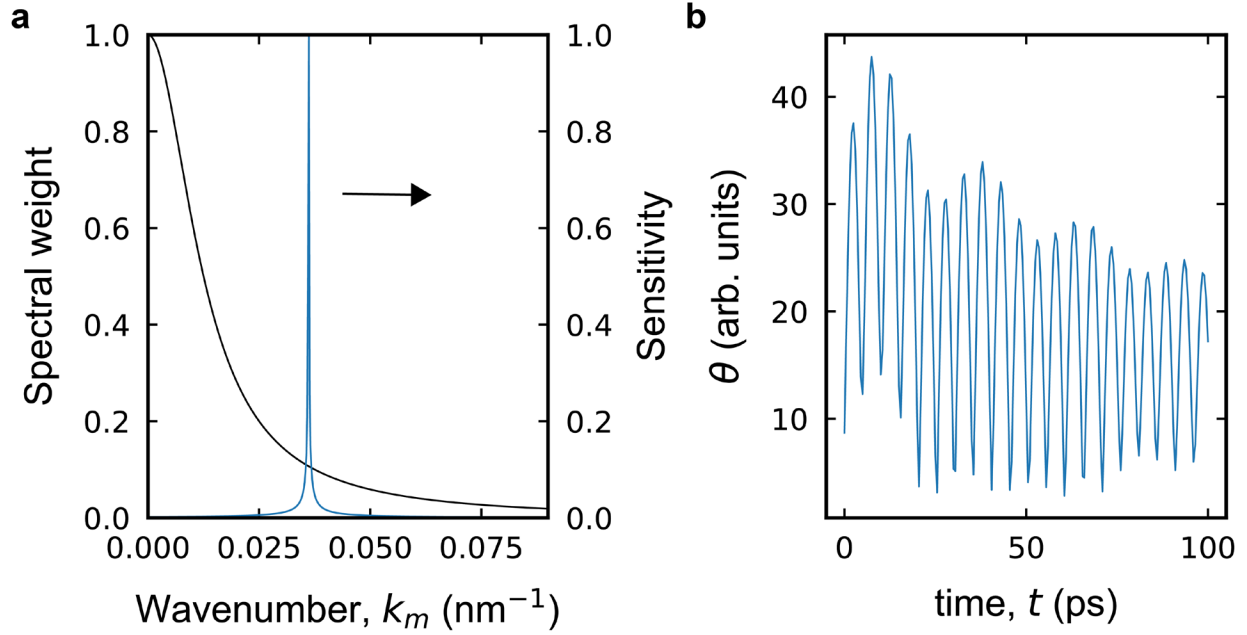
Supplementary Figure 2: **Wavenumber selectivity**. (**a**) Wavepacket distribution (black line, left axis) and the normalized sensitivity function as given Eq. S1.19 (blue line, right axis). (**b**) The resulting time-resolved MOKE signal, given by the wavepacket distribution and the sensitivity function from panel a). Damping parameter $\eta_m = 0.001$ nm^{-1}, wavepacket distribution: $a_k \sim \frac{1}{1+(k\delta)^2}$ (see Suppl. Section S2).

S2. Theoretical formalism on the generation of the magnon wavepacket

We describe the dynamics of the quasi-antiferromagnetic mode (q-AFM) in $DyFeO_3$ using the one-dimensional version of the sigma-model, which for the planar dynamics of the Néel vector can be obtained by the variation of the Lagrangian $L[\varphi]$:[2]

$$L[\varphi] = \int dz \left\{ \frac{A}{2} \left[\frac{1}{v_0{}^2} \left(\frac{\partial \varphi}{\partial t} \right)^2 - \left(\frac{\partial \varphi}{\partial z} \right)^2 \right] - w_a(\varphi) \right\}, \tag{S2.1}$$

where A is the non-uniform exchange constant, v_0 is the magnon speed at the linear region of the spectrum, $w_a(\varphi)$ is the anisotropy energy, and the angle $\varphi = \varphi(z,t)$ describes the deflection of the antiferromagnetic vector $\mathbf{L}$ from the equilibrium position (0° and 90° as measured from the y-axis in the collinear and canted AFM phase respectively, see Supplementary section S1). Note that the characteristic speed $v_0^2 = \gamma A \omega_{ex}/2M_0$ contains only terms of exchange origin, the uniform exchange parameter $\omega_{ex} = 2\gamma H_{ex}$ and the non-uniform exchange constant A, which results in the large value of this speed.

The general equation obtained from (S2.1) is the nonlinear Klein-Gordon equation (note that it transforms to the familiar sine Gordon equation for the variable 2φ for the simplest form of the anisotropy with only one constant, $w_a(\varphi) \propto \sin^2 \varphi$). In the linear approximation over the small deviations of φ from its equilibrium value it takes the universal form

$$\frac{\partial^2 \varphi}{\partial t^2} - v_0{}^2 \frac{\partial^2 \varphi}{\partial z^2} + \omega_0{}^2 \varphi = 0, \tag{S2.2}$$

where ω_0 is frequency of the spin-wave gap:

$$\omega_0{}^2 = \omega_{ex}\omega_a, \qquad \omega_a = \frac{\gamma}{2M_0} \frac{d^2 w_a}{d\varphi^2} \Big|_{\varphi=0}. \tag{S2.3}$$

The derivative of the anisotropy energy is calculated at the equilibrium value of φ, see for more details Ref. [7]. Thus, all the quantities can be present through two well-known quantities: the limiting group velocity $v_0 \approx 20$ km/s [8] and the value of the magnon gap ω_0, which is directly measured in our experiment. The characteristic space scale is given by the value v_0/ω_0.

Ultrashort pulses of light with a corresponding broadband optical spectrum are routinely being used as an instantaneous excitation to generate high frequency spin dynamics[9]. We start with the assumption that at the time $t = 0$, the spin deflection $\varphi(z,t)$ in the material is given by the spatial

profile of the optical excitation, schematically shown in Suppl. Fig. 3a, as the result of an instantaneous excitation (significantly shorter than the period of the spin precession):

$$\varphi(z, t = 0) = \begin{cases} \varphi_0 e^{-\frac{z}{\delta}} & z \geq 0 \\ 0 & z < 0 \end{cases}.$$ (S2.4)

Here, $z = 0$ forms the interface between the magnetic medium and vacuum, δ is the penetration depth of the excitation pulse and φ_0 the amplitude of the initial spin deflection, proportional to the pump fluence and inversely proportional to δ ($\varphi_0 \sim I/\delta$), as to conserve the total energy distributed among all the excited magnon modes.

In order to account for the boundary condition given by the surface of the sample, we consider the energy flow j_E; from the Lagrangian (Eq. S2.1) it follows:

$$j_E = -\frac{\partial L}{\partial(\partial\varphi/\partial z)}\frac{\partial\varphi}{\partial t} = -A\frac{\partial\varphi}{\partial z}\frac{\partial\varphi}{\partial t}.$$ (S2.5)

The energy flow should vanish at the surface ($z = 0$) at all times t. This gives the boundary condition $\frac{\partial\varphi}{\partial z}|_{z=0} = 0$ (free spins). The simplest way to find a solution obeying this boundary condition is to expand the problem symmetrically to $z < 0$, such that the solution of the symmetrical problem is $\tilde{\varphi}(z, t) = \tilde{\varphi}(-z, t)$ and can be found with the initial conditions:

$$\tilde{\varphi}(z, t = 0) = \varphi_0 e^{-\frac{|z|}{\delta}}$$ (S2.6a)

and

$$\frac{\partial\varphi}{\partial z}(z, t = 0) = \frac{\varphi_0}{\delta}\begin{cases} -e^{-\frac{z}{\delta}} & z \geq 0 \\ 0 & z = 0 \\ +e^{+\frac{z}{\delta}} & z < 0 \end{cases}$$ (S2.6b)

Using the dispersion relation of the material, which is obtained after solving Eq. S2.2, we obtain that for a given spin wave component ψ_k:

$$\psi_k(z, t) = A e^{ikz - i\omega_k t} + B e^{ikz + i\omega_k t}, \qquad \omega_k = \sqrt{\omega_0^2 + (v_0 k)^2}$$ (S2.7)

Here, as before, $\omega_0 = \sqrt{\omega_{ex}\omega_a}$ the spin wave gap and v_0 the characteristic speed. Having in mind the symmetry of the wanted solution, the only solution which is symmetric over inversion of the magnon eigenmodes, is:

$$\psi_k(z,t) = C_k \cos(kz)\cos(\omega_k t) \tag{S2.8}$$

From Eq. (S2.6a) we can write the spin deflection $\tilde{\varphi}(z, t = 0)$ in a material slab of thickness d using the Fourier expansion as:

$$\tilde{\varphi}(z, t = 0) = \varphi_0 \sum_k a_k e^{ikz} ,$$

$$a_k = \frac{1}{d}\frac{2\delta}{1 + (\delta k)^2} \tag{S2.9}$$

From this expression we find that the initial exponential distribution in spin-deflection in real-space corresponds to a broadband magnon wavepacket, as shown in Suppl. Fig. 3b.

Then in the continuous limit $(d \to \infty)$, combining Eq. (S2.4) and Eq. (S2.9) we can easily obtain the final expression, given in the manuscript:

$$\varphi(z,t) = \tilde{\varphi}(z \geq 0, t) = \frac{2\varphi_0}{\pi} \int_{-\infty}^{\infty} dk \left[\frac{\delta}{1 + (k\delta)^2}\cos(kz)\cos(\omega_k t)\right]; \quad (z \geq 0), \varphi_0 \sim \frac{I_0}{\delta} \tag{S2.10}$$

$$= \frac{2}{\pi} \int_{-\infty}^{\infty} dk[A_k \cos(kz)\cos(\omega_k t)]; \quad A_k = \frac{1}{d}\frac{\delta}{1 + (\delta k)^2}$$

Eq. S2.10 describes the spin deflection as a function of space (z) and time (t) and therefore the dynamics of the broadband magnon wavepacket which will start propagating into the sample. This is shown in Fig. 4a in the main text.
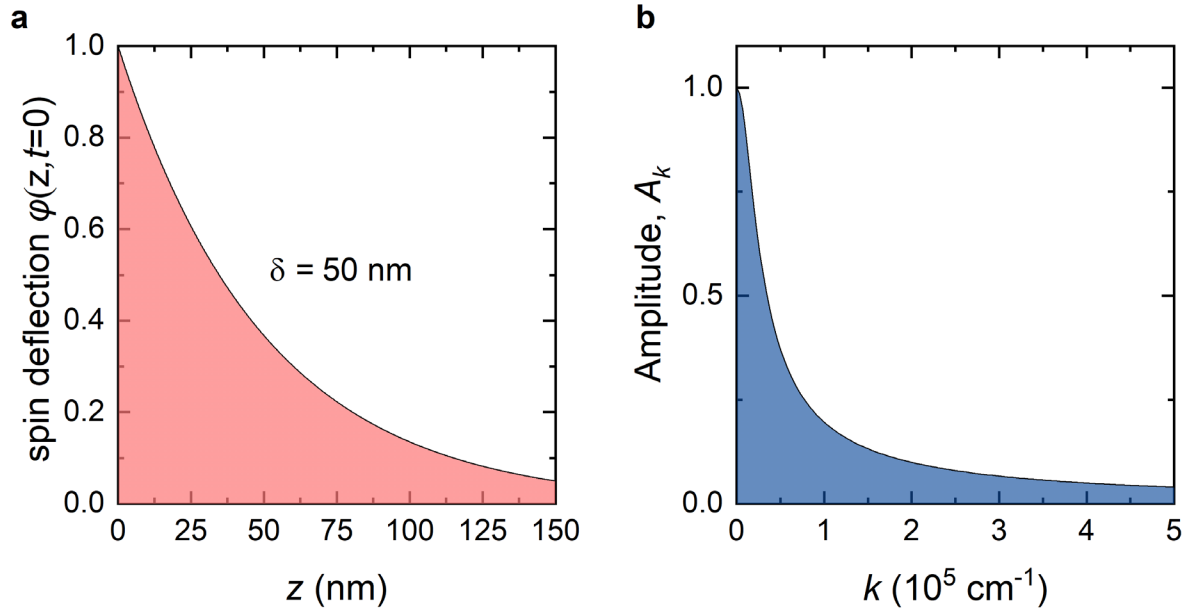
Supplementary Figure 3: Real-space wavevector spin deflection distribution. (a,b) Real-space distribution of the spin deflection $\varphi(z,t)$ (a) and the corresponding wavevector distribution (b).

S3. Excitation of a propagating wavepacket of coherent acoustic phonons

Following the excitation with pump pulses at a photon energy of hv = 3.1 eV, the time-resolved polarization rotation signal θ_K reveals oscillatory dynamics at two central frequencies (see Suppl. Fig. 4a). As argued in the main text, the high-frequency component corresponds to a finite-k magnon mode. The slow-varying component is caused by a broadband wavepacket of propagating acoustic phonons as in details described in Ref. [5]. The generation and detection of ultrafast light-induced coherent acoustic phonons in solids is a well-established research field known as picosecond acoustics[10]. Typically, the generation is based on a conversion of the energy of the strongly absorbed ultrashort pump pulse into photo-induced stress in vicinity of the material surface[10]. The stress leads to modulation of the intensity of light reflected from the sample as a consequence of modulation of refractive index due to optoacoustic effects. The acoustic wavepacket observed in our experiments is seen as oscillations in the probe pulse polarization rotation, which is also proportional to the intensity of reflected light.

More generally, the opto-acoustic conversion process can be described similarly to the magnon detection outlined in Supplementary section S1, which causes the probe pulse to be specifically sensitive to an acoustic phonon with the wavenumber given by Eq. S1.22[11]. The frequency of the resulting oscillation corresponds to the intrinsic frequency of the acoustic phonon. Therefore the measured oscillations can be used to map out the phonon dispersion, just like it is done in Fig. 4 of the main text for the magnon dispersion. We extract the central frequency of the slow oscillations for the different probing wavelengths that are also used in Figure 4. These frequencies are plotted for the wavenumber calculated using Eq. S1.22 and shown in Suppl. Fig. 4b with a linear dispersion fit. The velocity of the sound waves extracted from this fit is v_s = 6.2 km/s. This agrees well with literature values of the longitudinal sound velocity in the orthoferrites, which all lie in the range of about 6.0-6.5 km/s at cryogenic temperatures[12-14]. We therefore conclude that optical excitation of the strongly-absorbing charge-transfer transitions excites both a propagating broadband magnon wavepacket and a propagating broadband acoustic phonon wavepacket.
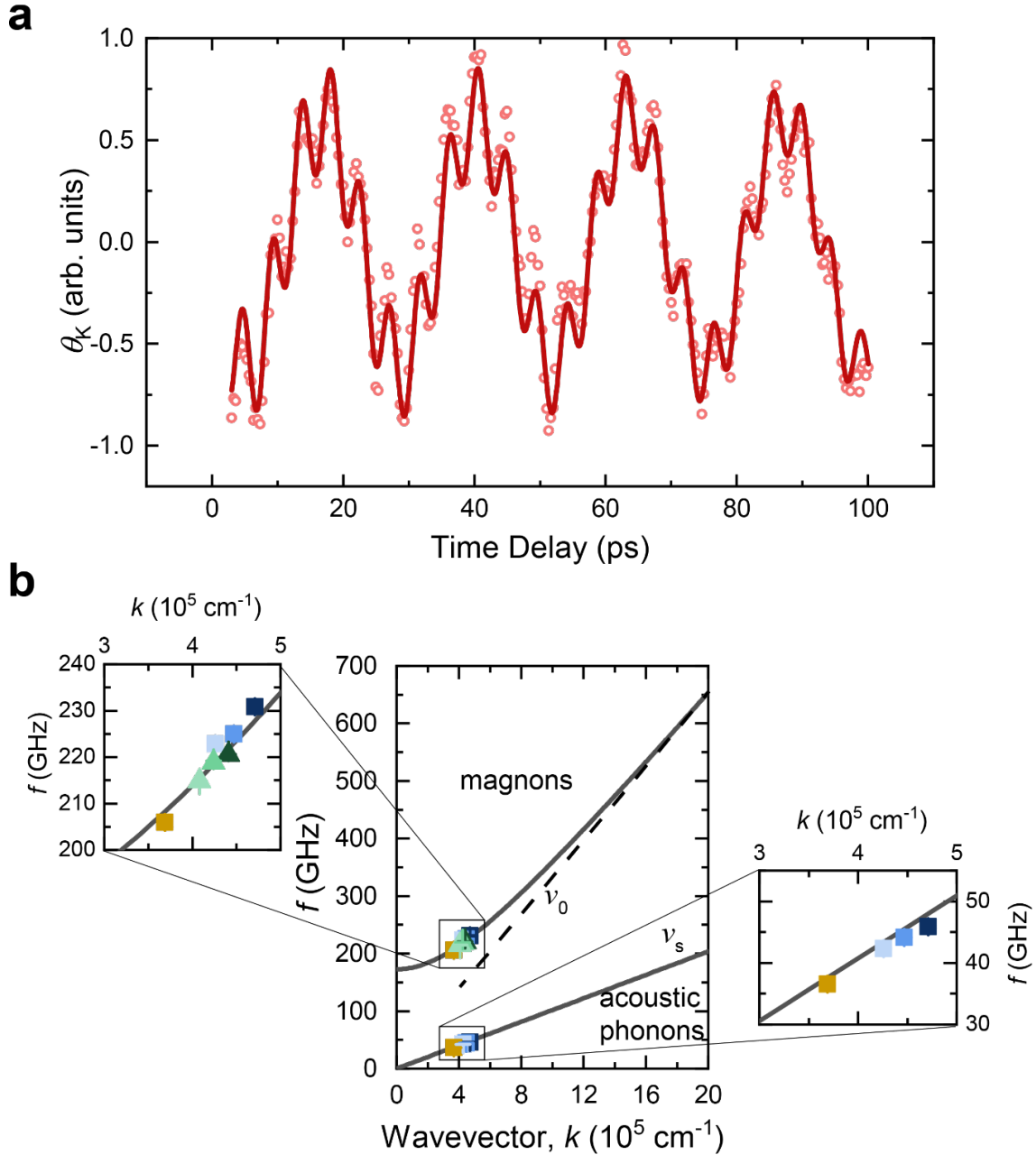
Supplementary Figure 4: Observation of a wavefront of propagating acoustic phonons. (**a**) Time resolved polarization rotation in the reflection geometry following excitation at $h\nu = 3.1$ eV, $T = 60$ K. The solid line represents a best fit using a double-sine function. The slower oscillations are the result of a finite-k phonon mode. The higher frequency oscillation corresponds to a finite-k magnon mode. (**b**) Dispersion relation for the magnons, where the slope of the dispersion defines the (limiting) propagation speed of the waves, with the datapoints from Fig. 4 main text. The extracted phonon frequencies are plot against the wavenumber calculated using Eq. S1.22 and fit with a linear dispersion, which then represents the (longitudinal) acoustic phonon branch in $DyFeO_3$.

14

## S4. Temperature and magnetic field dependence of the magnon and phonon modes

To further investigate the behavior of the detected finite-k waves (see Supplementary Section S3) we studied their excitation at different temperatures across the Morin phase transition (see Suppl. Fig. 5a). From the Fourier spectra of these signals (see Suppl. Fig. 5b), we can distinguish clear contributions from the acoustic phonon mode (~40 GHz) and magnon mode (>200 GHz) at all temperatures.

Another way to confirm the attribution of the slow oscillation to an acoustic phonon mode and the fast oscillation to a magnon mode is to perform the measurements in a magnetic field. In the WFM phase, a magnetic field can bias the orientation of the small net magnetic moment of $DyFeO_3$. As shown in Suppl. Fig. 6, there is a strong dependence of the magnon amplitude on the polarity of the applied field in contrast to the phonon mode.
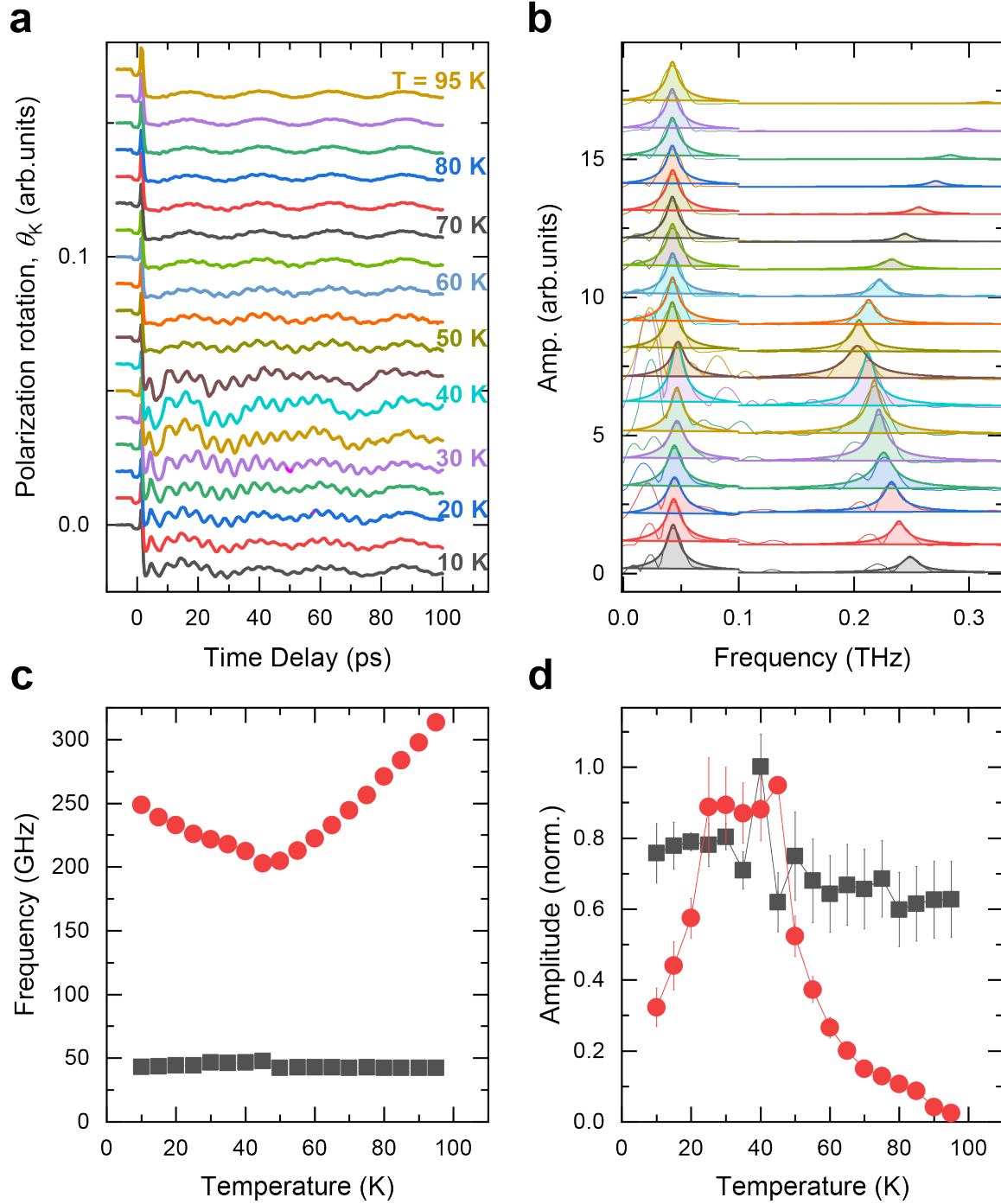
Supplementary Figure 5: Temperature dependence of the magnon and phonon modes. (**a**) Time-resolved measurements of the polarization rotation θ_K of a probe pulse ($\lambda_0 = 700$ nm) for different temperatures. (**b**) The FFT spectra of the time-domain signals from panel (a). The peaks corresponding to the phonon and magnon mode are fit with Lorentzians. (**c,d**) The frequency (c) and amplitude (d) of the oscillatory components corresponding to the magnon and phonon mode, extracted with the Lorentzian fits in panel (b). Red spheres: magnon data, black squares: phonon data.
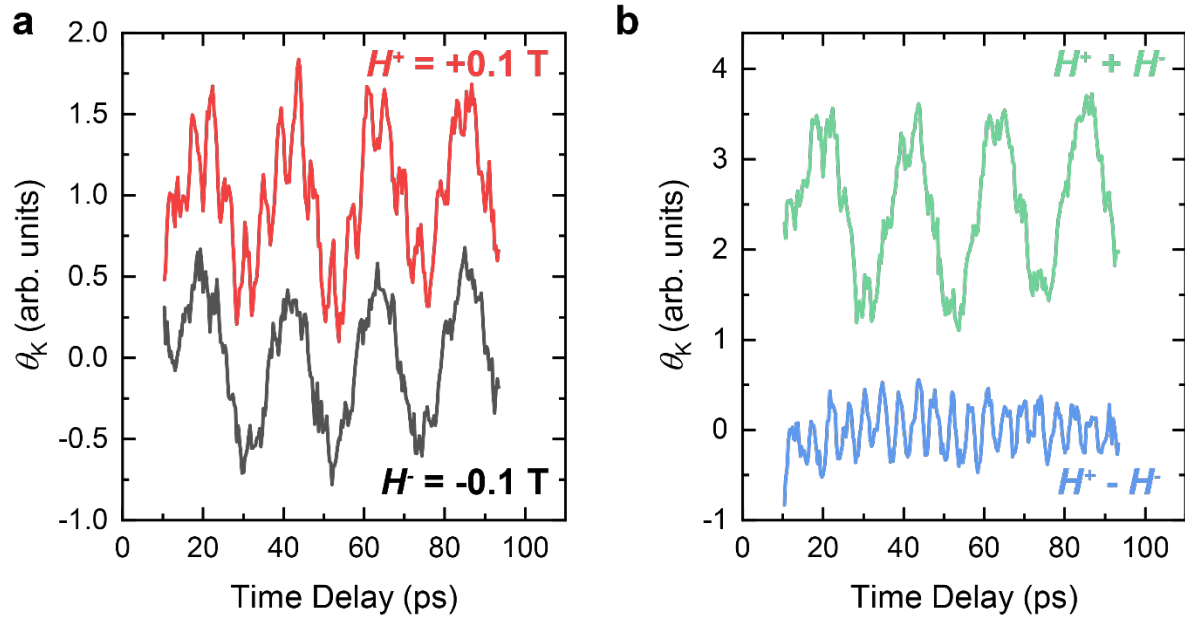
Supplementary Figure 6: Magnetic field dependence. (**a**) Time-resolved measurements of the polarization rotation θ_K of a probe pulse ($\lambda_0 = 800$ nm) after excitation with pump pulses ($h\nu = 3.1$ eV) in magnetic fields with opposite polarity. (**b**) The sum and difference of the signals from panel (a) highlighting the phonon and magnon mode respectively.

S5. Polarization dependence of the magnon and phonon modes

The results of the measurements for different probe polarization orientations are summarized in Suppl. Fig. 7. The polarization dependence of the amplitude of the measured oscillation corresponding to the magnon and phonon modes are substantially different. Whereas the phonon amplitude peaks for a probe polarization right in-between the crystal x- and y-axis ($\alpha = +45, +135$) and undergoes a 180° phase shift (see Suppl. Fig. 7a), the magnon amplitude is less sensitive to the orientation and largest for the polarization oriented along the crystallographic x and y axis. We also note that in vicinity of T_M the amplitude spectra reveal a probe polarization-dependent peak (mode 1) at a low frequency (~12 GHz), of which the origin remains to be identified.

The pump polarization of the excitation pulse has a profound effect on the amplitude and phase of the excited spin dynamics. As shown in Suppl. Fig. 8, there is a slight change in phase as the pump polarization changes and a large change in the measured amplitude.
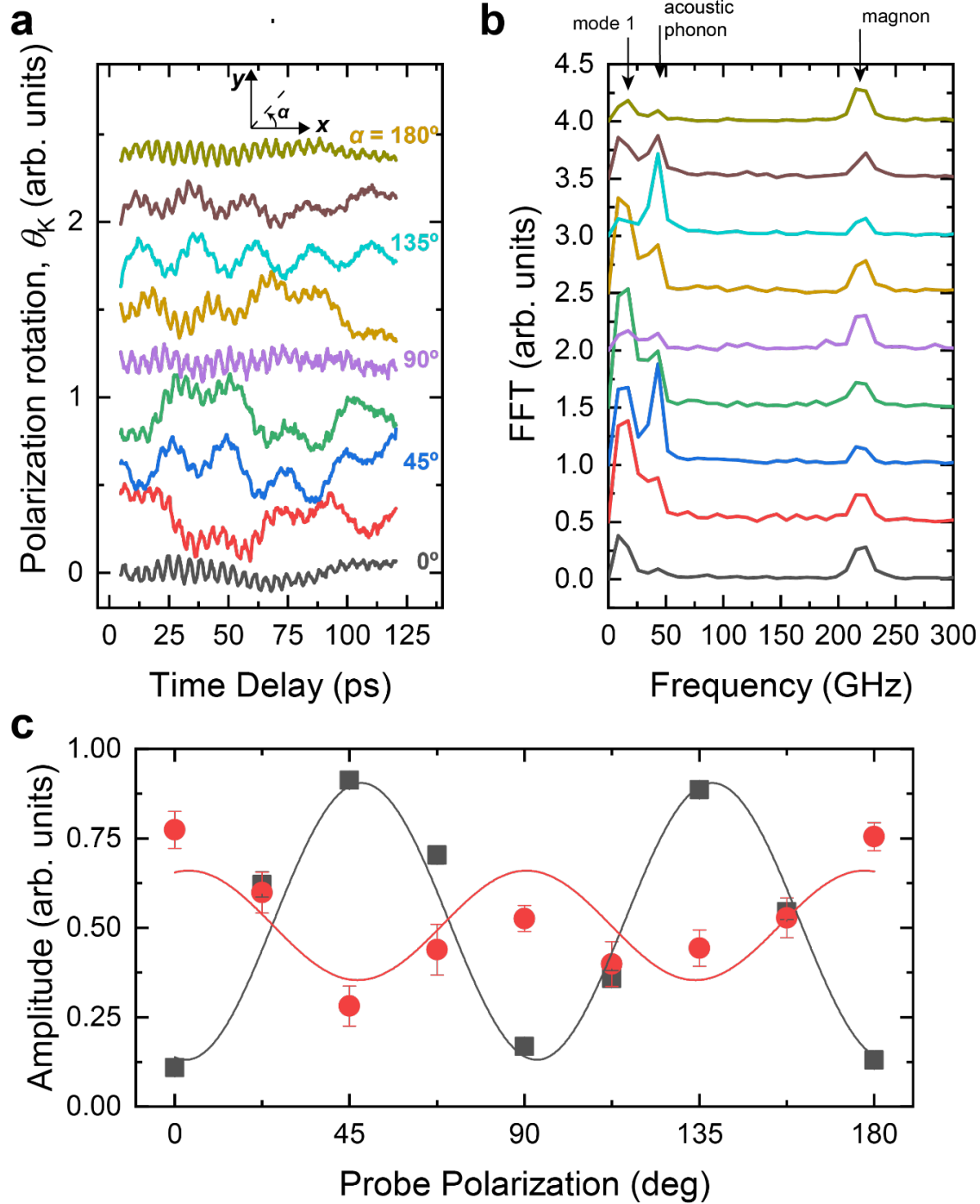
Supplementary Figure 7: Detection of finite-*k* magnon and phonon modes for different orientations of the probe polarization. (**a**) Time-resolved measurements of the polarization rotation $\Delta\theta_K$ of a probe pulse ($\lambda_0 = 690$ nm) for different orientations of the probe polarization plane w.r.t. the crystallographic *x*-axis. (**b**) The Fourier spectra of the time-domain signals from panel (a) and the peaks attributed to different modes. (**c**) The amplitude of the oscillatory components corresponding to the magnon and phonon mode for the different probe polarizations. The amplitudes are determined by fitting the data from panel (a) with a function with three sine functions with frequencies corresponding to the magnon, phonon and mode 1. The solid lines are guides to the eye to highlight the amplitude response to changes in the orientation of the probe polarization plane.
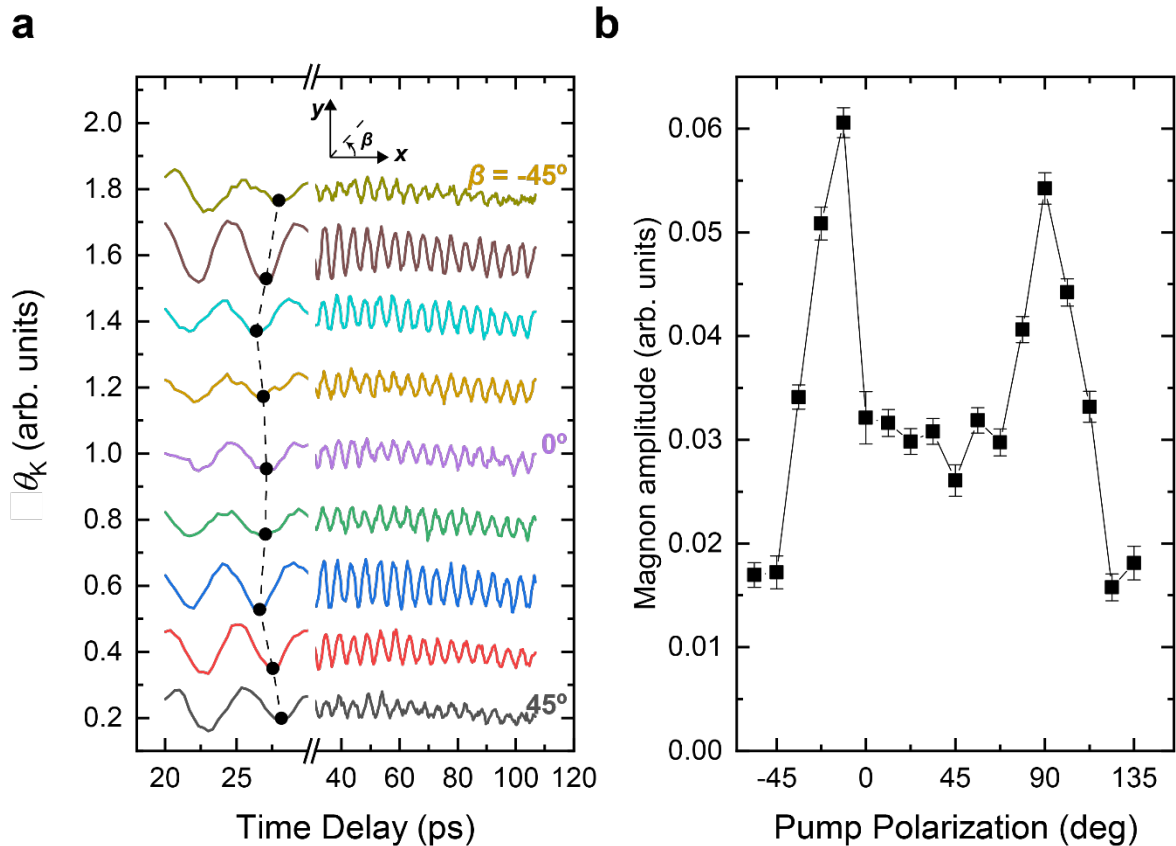
Supplementary Figure 8: Pump polarization dependence. (**a**) Time-resolved measurements of the polarization rotation θ_K of a probe pulse ($\lambda_0 = 800$ nm) for different orientations of the pump polarization plane ($h\nu = 3.1$ eV) w.r.t. the crystallographic x-axis. The connected points show the temporal position of the magnon minimum (phase) for each pump polarization. (**b**) The amplitude of the oscillatory component corresponding to the magnon mode for the different orientations of the pump polarization plane. The amplitudes are determined by fitting the data from panel (a) with a sine function.

References

1   Bar'yakhtar, V. G., Ivanov, B. & Sukstanskii, A. L. Nonlinear waves and the dynamics of domain walls in weak ferromagnets. *Zh. Eksp. Teor. Fiz* **78**, 1509-1522 (1980).

2   Galkina, E. & Ivanov, B. Dynamic solitons in antiferromagnets. *Low. Temp. Phys.* **44**, 618-633 (2018).

3   Zvezdin, A. & Matveev, V. Theory of the magnetic properties of dysprosium orthoferrite. *Sov. Phys. JETP* **50**, 543-548 (1979).

4   Balbashov, A., Volkov, A., Lebedev, S., Mukhin, A. & Prokhorov, A. High-frequency magnetic properties of dysprosium orthoferrite. *Zh. Eksp. Teor. Fiz. [Sov. Phys. JETP]* **88**, 974-987 (1985).

5   Thomsen, C., Grahn, H. T., Maris, H. J. & Tauc, J. Surface generation and detection of phonons by picosecond light pulses. *Phys. Rev. B* **34**, 4129 (1986).

6   Zvezdin, A. K. & Kotov, V. A. *Modern magnetooptics and magnetooptical materials.* (CRC Press, 1997).

7   Afanasiev, D. *et al.* Control of the ultrafast photoinduced magnetization across the Morin transition in DyFeO$_3$. *Phys. Rev. Lett.* **116**, 097401 (2016).

8   Bar'yakhtar, V. G., Ivanov, B. & Chetkin, M. V. Dynamics of domain walls in weak ferromagnets. *Sov. Phys. Usp.* **28**, 563-588 (1985).

9   Němec, P., Fiebig, M., Kampfrath, T. & Kimel, A. V. Antiferromagnetic opto-spintronics. *Nat. Phys.* **14**, 229-241 (2018).

10   Ruello, P. & Gusev, V. E. Physical mechanisms of coherent acoustic phonons generation by ultrafast laser action. *Ultrasonics* **56**, 21-35 (2015).

11   Babilotte, P. *et al.* Femtosecond laser generation and detection of high-frequency acoustic phonons in GaAs semiconductors. *Phys. Rev. B* **81**, 245207 (2010).

12   Gorodetsky, G. & Lüthi, B. Sound-Wave—Soft-Mode Interaction near Displacive Phase Transitions: Spin Reorientation in ErFeO$_3$. *Phys. Rev. B* **2**, 3688 (1970).

13   Gorodetsky, G., Shaft, S. & Wanklyn, B. Magnetoelastic properties of TmFeO$_3$ at the spin reorientation region. *Phys. Rev. B* **14**, 2051 (1976).

14   Tsymbal, L. T. & Isotov, A. I. Features of acoustic properties of ErFeO$_3$ in second-order phase transitions. *Sov. Phys. JETP* **75**, 525-531 (1992).